catalysts

MDPI

Article

Visible-Light Photocatalytic Degradation of Naproxen and Ibuprofen over Two-Dimensional Bi_2MoO_6 Nanosheets: Mechanism, Transformation Pathways, and Changes in Toxicity

Kun Fu [1,2,*], Huiping Deng [3], Pujing Yao [2], Pengkang Jin [1], Yuan Liu [2], Minquan Feng [4], Ning Luo [2] and Huan Ma [2]

1 School of Human Settlements and Civil Engineering, Xi'an Jiaotong University, Xi'an 710049, China; pkjin@xjtu.edu.cn
2 PowerChina Northwest Engineering Corporation Limited, Xi'an 710065, China
3 College of Environmental Science and Engineering, Tongji University, Shanghai 200092, China; denghuiping@tongji.edu.cn
4 State Key Laboratory of Water Engineering Ecology and Environment in Arid Area, Xi'an Polytechnic University, Xi'an 710048, China; mqfeng@xaut.edu.cn
* Correspondence: fukun_nwh@163.com

Abstract

Visible-light photocatalysis offers a potential route for removing pharmaceutical contaminants from water. However, parent-compound removal alone may not adequately reflect treatment performance, particularly with respect to mineralization and toxicity. Here, two-dimensional Bi_2MoO_6 nanosheets (BMO-nanosheet) were synthesized by a hydrothermal method and compared with bulk Bi_2MoO_6 (BMO-bulk). BMO-nanosheet exhibited a higher BET specific surface area, while photoelectrochemical measurements suggested more efficient charge separation and transfer. Following 60 min of dark adsorption and 60 min of visible-light irradiation ($\lambda > 420$ nm), overall removal of naproxen (NPX) and ibuprofen (IBP) by BMO-nanosheet reached approximately 91% and 90%, respectively. The irradiation-stage apparent rate constants were 3.1 and 4.7 times those of BMO-bulk, respectively. Similar removal was observed over five cycles at a fixed catalyst dosage. In separate experiments without preliminary dark equilibration, removal in spiked reservoir water reached approximately 69% for NPX and 52% for IBP after 60 min of irradiation. Under the direct-irradiation protocol, aqueous total organic carbon removal reached 34% and 70% for NPX and IBP, respectively, indicating incomplete mineralization despite substantial parent-compound removal. EPR and scavenger results supported the involvement of h^+ and $^1O_2$, with a possible contribution from $O_2^{\bullet-}$ to NPX degradation. Seven NPX and nine IBP transformation products were tentatively identified by LC–MS/GC–MS, and conceptual DFT descriptors aided interpretation of the proposed pathways. CHO-K1 cell viability initially decreased and then partially recovered with longer irradiation. Separately, ECOSAR predicted greater aquatic toxicity for some proposed products than for their parent compounds. These findings suggest the potential of BMO-nanosheet for visible-light-driven pharmaceutical removal and highlight the importance of evaluating mineralization and toxicity alongside parent-compound removal.

Keywords: Bi_2MoO_6 nanosheets; nonsteroidal anti-inflammatory drugs; visible-light photocatalysis; transformation pathways; toxicity evolution

Check for updates

Academic Editor: Akira Nishimura

Received: 18 September 2026
Revised: 4 November 2026
Accepted: 11 November 2026
Published: 18 November 2026

Copyright: © 2026 by the authors. Licensee MDPI, Basel, Switzerland. This article is an open access article distributed under the terms and conditions of the Creative Commons Attribution (CC BY) license.

1. Introduction

Naproxen (NPX) and ibuprofen (IBP) are widely used non-steroidal anti-inflammatory drugs (NSAIDs). Their extensive use, incomplete metabolism, and variable removal during conventional wastewater treatment contribute to their continuous release into receiving waters [1–4]. Although environmental concentrations are generally much lower than those used in laboratory kinetic experiments, chronic exposure and mixture effects remain a concern because NSAIDs can affect oxidative homeostasis, development, reproduction, and endocrine function in aquatic organisms [5,6]. Parent-compound removal alone may not adequately describe treatment performance, as partial oxidation can generate transformation products with different persistence and toxicity. Dissolved organic matter and inorganic ions in natural waters may further influence reaction rates and product formation.

Visible-light heterogeneous photocatalysis offers a means of transforming refractory organic contaminants under mild conditions [7]. Its efficiency can be constrained by limited light utilization, electron–hole recombination, charge transport to surface reaction sites, and scavenging by water-matrix constituents [8,9]. Two-dimensional semiconductor nanosheets provide opportunities to improve charge transport and interfacial reactions through shorter transport distances and greater exposure of surface sites [10]. These potential advantages motivate comparisons with bulk counterparts, although improved photocatalytic activity does not necessarily imply a corresponding increase in mineralization or a reduction in toxicity.

Bi_2MoO_6 is a layered, visible-light-responsive Aurivillius oxide whose structural and electronic properties have attracted interest in photocatalysis and related applications [11–19]. Stacking and aggregation can limit the accessibility of its surfaces and may hinder effective use of photogenerated carriers. Previous studies have shown that morphology control, atomic-scale thinning, and interface engineering can modify carrier dynamics and surface reactivity [10,12,16,17,20,21]. Specifically, reducing the thickness of Bi_2MoO_6 nanosheets may shorten the migration distance of photogenerated carriers to the surface, whereas reducing sheet stacking may improve access to surface reaction sites. These potential advantages provide a basis for comparing the photocatalytic performance of Bi_2MoO_6 nanosheets with that of the bulk reference. Layered photocatalysts have also been investigated for the visible-light degradation of NPX and other organic contaminants [22–24]. An important question for Bi_2MoO_6 nanosheets is whether enhanced removal of structurally distinct NSAIDs is accompanied by favorable changes in mineralization and toxicity and how these outcomes are affected by the water matrix.

Here, we used cetyltrimethylammonium bromide (CTAB) to assist the one-step hydrothermal synthesis of two-dimensional Bi_2MoO_6 nanosheets, with Bi_2MoO_6 prepared without CTAB as the bulk reference. NPX and IBP were selected as representative NSAIDs because of their widespread use, environmental relevance, and distinct molecular structures. NPX contains a methoxy-substituted naphthalene moiety, whereas IBP contains an isobutyl-substituted benzene ring. Comparing these two compounds under identical photocatalytic conditions allows us to examine how degradation behavior, transformation pathways, mineralization, and toxicity evolution differ between structurally distinct pollutants within the same pharmaceutical class. Structural and photoelectrochemical characterization was combined with degradation experiments to examine possible relationships between material properties and activity. Water-chemistry effects, catalyst reuse, and treatment in spiked reservoir water were assessed alongside mineralization. EPR spin trapping and scavenger experiments provided evidence on reactive-species contributions, while LC–MS/GC–MS analyses and conceptual DFT descriptors informed the proposed transformation pathways. CHO-K1 assays tracked changes in cytotoxicity during treatment; ECOSAR separately estimated the aquatic toxicity of individual parent compounds and

proposed products. Building on previous studies of Bi_2MoO_6 morphology and visible-light NPX degradation [16,17,20–23], this study compares nanosheet and bulk Bi_2MoO_6 for the treatment of two structurally distinct NSAIDs while jointly examining parent-compound removal, mineralization, and toxicity evolution. Its specific contribution is to assess whether enhanced pharmaceutical removal is accompanied by comparable improvements in mineralization and cytotoxicity, with transformation-product analysis and separate aquatic-toxicity predictions supporting the interpretation. Experiments in spiked reservoir water further assess how the water matrix influences treatment performance.

2. Results and Discussion

2.1. Morphology, Crystal Phase, and Surface Chemistry

SEM images show plate-like particles in both samples (Figure S1). BMO-bulk consists of relatively thick, densely aggregated plates, whereas BMO-nanosheet contains thinner, more open lamellae with less stacking. TEM further distinguishes the two morphologies: BMO-bulk is strongly aggregated and contains few clearly separated sheets, whereas BMO-nanosheet forms well-defined, thin rectangular lamellae (Figure 1). HRTEM images show lattice fringes with a spacing of 0.275 nm, which is assigned to the Bi_2MoO_6 (200) plane [17]. These observations suggest that CTAB promotes anisotropic growth while limiting stacking and aggregation. AFM images and corresponding height profiles showed local height differences of approximately 8.65 nm for BMO-bulk and 5.26 nm for BMO-nanosheet at the selected positions (Figure S2). BMO-nanosheet also exhibited a higher BET specific surface area (23.52 $m^2\ g^{-1}$) than BMO-bulk (18.00 $m^2\ g^{-1}$), which may facilitate pollutant–catalyst contact (Table S1).

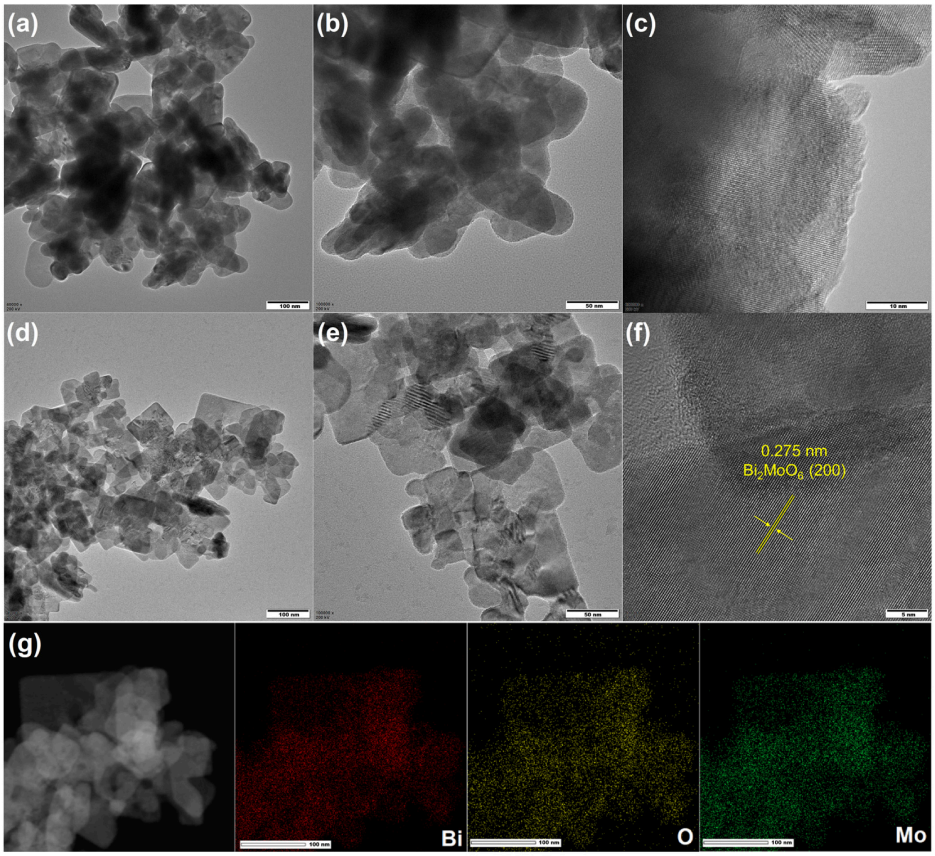


Figure 1. (**a**–**c**) TEM and HRTEM images of BMO-bulk; (**d**–**f**) TEM and HRTEM images of BMO-nanosheet; and (**g**) electron micrograph and corresponding EDX maps of Bi, O, and Mo in BMO-nanosheet (left to right). The lattice spacing of 0.275 nm in (**f**) is assigned to the Bi_2MoO_6 (200) plane.

The XRD patterns of both samples are consistent with orthorhombic Bi_2MoO_6 (JCPDS 21-0102). Representative reflections at approximately 10.9°, 28.3°, 33.1°, and 58.5° correspond to the (020), (131), (060), and (262) planes, respectively (Figure 2). The peak groups near 32.6°, 47°, and 55.5° contain closely spaced reflections, as indicated by the reference pattern. Differences in the relative diffraction intensities between BMO-nanosheet and BMO-bulk may reflect differences in preferred orientation [16,20,21]. The apparent crystallite sizes were estimated from the (131) reflection using the Scherrer equation, $D = K\lambda/(\beta\cos\theta)$, where K is the shape factor, λ is the X-ray wavelength, β is the full width at half maximum (FWHM) in radians, and θ is the Bragg angle. The peak profiles were fitted using a pseudo-Voigt function with a linear background. Taking $K = 0.9$ and $\lambda = 0.15406$ nm, the fitted FWHM values of 0.4541° and 0.3164° yielded apparent crystallite sizes of approximately 18.0 and 25.9 nm for BMO-nanosheet and BMO-bulk, respectively. These estimates suggest a smaller coherent diffraction domain size normal to the (131) planes in BMO-nanosheet. These values represent approximate apparent crystallite sizes, as instrumental broadening and microstrain contributions were not separated.

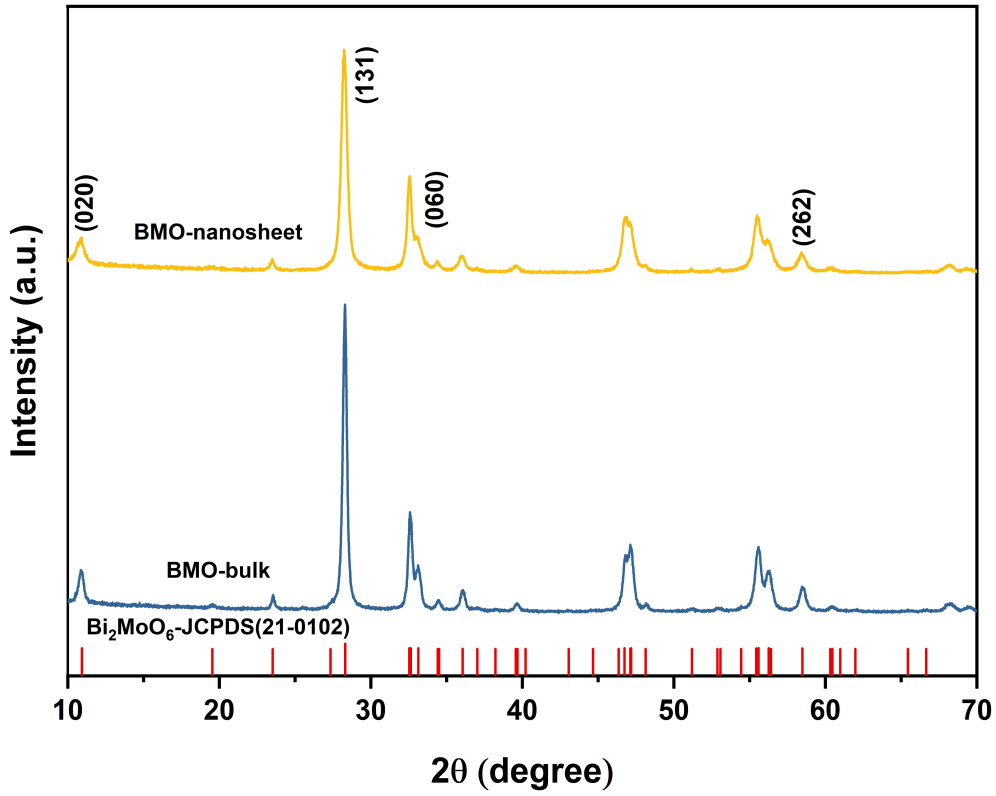


Figure 2. XRD patterns of BMO-bulk and BMO-nanosheet.

EDX maps show that Bi, Mo, and O are distributed throughout BMO-nanosheet, with no obvious microscale segregation (Figure 1g). The XPS survey spectra (Figure 3a) exhibit additional prominent features assigned to Bi 5d near 26 eV, Mo 3p at approximately 398 and 416 eV, Bi 4d at approximately 442 and 466 eV, and Bi $4p_{3/2}$ near 681 eV. The feature at approximately 973–974 eV corresponds to the O KLL Auger signal. These features originate from the constituent elements of Bi_2MoO_6. The high-resolution XPS spectra show Mo^{6+} components at 232.4 and 235.6 eV (Mo $3d_{5/2}$ and Mo $3d_{3/2}$), Bi^{3+} components at 158.8 and 164.1 eV (Bi 4f), and lattice and adsorbed oxygen components at 530.12 and 531.60 eV (O 1s) (Figure 3) [16,24]. The small shifts of the Bi 4f and Mo 3d peaks in opposite directions relative to BMO-bulk suggest changes in the local coordination and electronic environment of the nanosheet sample [17].

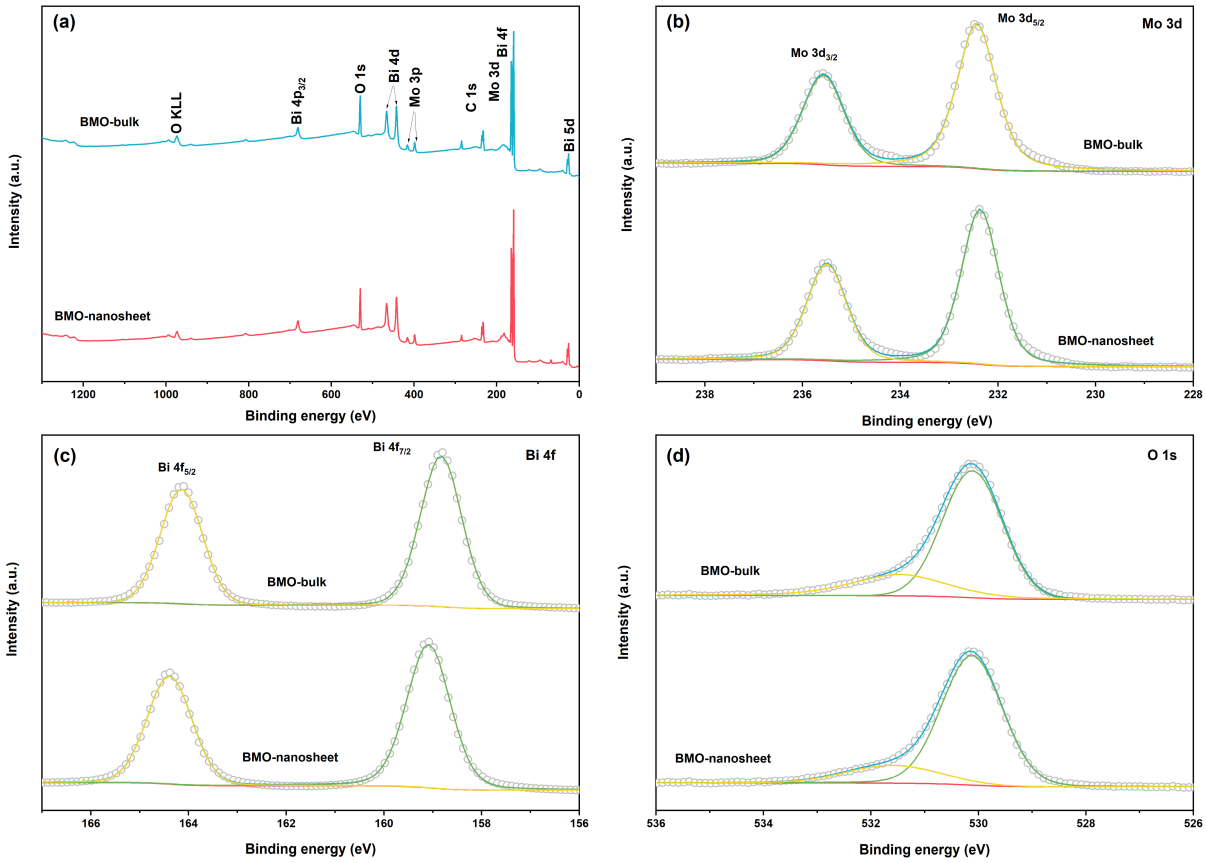


Figure 3. XPS spectra of BMO-nanosheet and BMO-bulk: (**a**) survey spectra; (**b**) high-resolution Mo 3d spectra; (**c**) high-resolution Bi 4f spectra; and (**d**) high-resolution O 1s spectra.

2.2. Optical Properties, Band Energetics, and Charge-Transfer Behavior

Figure 4 summarizes the optical and photoelectrochemical properties of the two materials. Both absorb visible light up to approximately 520 nm (Figure 4a). Tauc analysis gives band gaps of 2.43 eV for BMO-bulk and 2.49 eV for BMO-nanosheet (Figure 4b), indicating that the higher activity of BMO-nanosheet is not caused by band-gap narrowing. The positive slopes of the Mott–Schottky plots indicate n-type behavior. The flat-band potentials were approximated from the extrapolated intercepts as −0.46 and −0.85 V versus Ag/AgCl for BMO-bulk and BMO-nanosheet, respectively (Figure 4c). These potentials were converted to the normal hydrogen electrode (NHE) scale using E(NHE) = E(Ag/AgCl) + 0.197 V for a saturated-KCl Ag/AgCl reference electrode at 25 °C. Assuming that the conduction-band potentials are 0.10 V more negative than the flat-band potentials, the conduction-band positions were estimated to be −0.36 and −0.75 V versus NHE, respectively. Combining these estimates with the corresponding band gaps of 2.43 and 2.49 eV yielded valence-band potentials of 2.07 and 1.74 V versus NHE, respectively [25]. The more negative conduction-band position of BMO-nanosheet is expected to favor reduction reactions. Relative to BMO-bulk, BMO-nanosheet showed lower PL intensity (Figure 4d) and a larger photocurrent response during repeated light on/off cycles (Figure 4e). Under illumination, equivalent-circuit fitting of the EIS spectra (Figure 4f) yielded a lower apparent charge-transfer resistance (Rct) for BMO-nanosheet (approximately 281 Ω) than for BMO-bulk (approximately 314 Ω). The equivalent circuit and fitted curves are shown in Figures S3 and S4, respectively, and the fitted Rct values are listed in Table S2. Together, these results are consistent with more efficient charge separation and interfacial charge transfer in BMO-nanosheet under the measurement conditions.

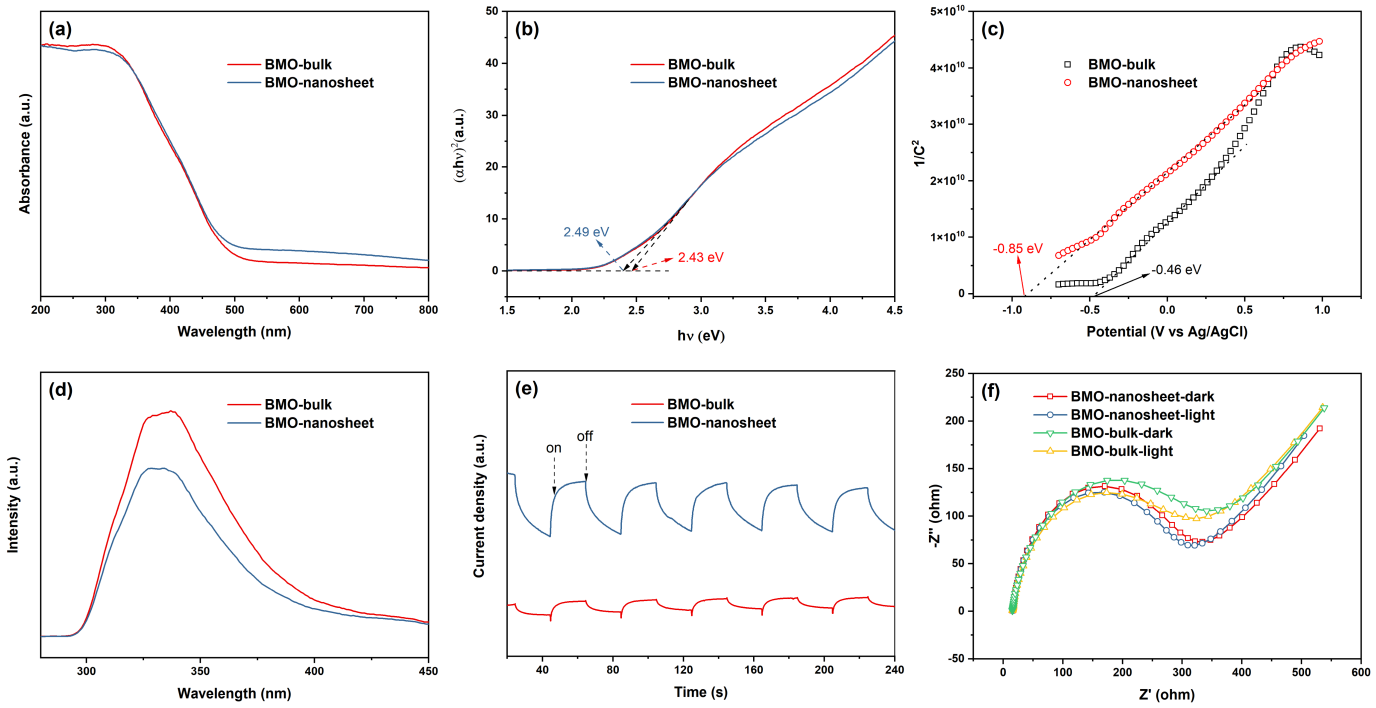


Figure 4. Optical and photoelectrochemical properties of BMO-bulk and BMO-nanosheet: (**a**) UV–vis spectra; (**b**) corresponding Tauc plots; (**c**) Mott–Schottky plots; (**d**) photoluminescence spectra; (**e**) transient photocurrent responses under repeated light on/off cycles; and (**f**) EIS Nyquist plots under dark and illuminated conditions.

2.3. Visible-Light Degradation of NPX and IBP

2.3.1. Activity and Kinetics

Neither NPX nor IBP underwent appreciable degradation during 60 min of visible-light irradiation in the absence of a catalyst (Figure S5). The catalyst-comparison experiments included 60 min of dark adsorption followed by 60 min of visible-light irradiation. BMO-nanosheet exhibited greater dark adsorption than BMO-bulk, and the aqueous concentrations of both pollutants decreased further after illumination (Figure 5a,b). At the end of the combined adsorption–irradiation treatment, overall removal relative to the initial concentration before dark adsorption reached approximately 72% and 91% for NPX over BMO-bulk and BMO-nanosheet, respectively, and 49% and 90% for IBP. These overall removal efficiencies include both dark adsorption and subsequent removal under irradiation.

The irradiation-stage kinetics were evaluated using the measured aqueous concentration at the onset of illumination as C_0 (Figure 5c,d). Apparent pseudo-first-order rate constants were 0.019 and 0.059 min^{-1} for NPX over BMO-bulk and BMO-nanosheet, respectively, and 0.010 and 0.046 min^{-1} for IBP (Table S3). Based on the unrounded fitted values, the corresponding nanosheet-to-bulk rate-constant ratios were approximately 3.1 and 4.7 for NPX and IBP, respectively. The higher apparent rates for BMO-nanosheet are consistent with its photoelectrochemical response and less aggregated morphology, rather than band-gap narrowing.

Table S4 compares these results with previously reported photocatalytic systems. BMO-nanosheet achieved substantial NPX and IBP removal at a catalyst dosage of 0.20 g L^{-1}. Differences in experimental conditions should be considered when comparing performance across studies.

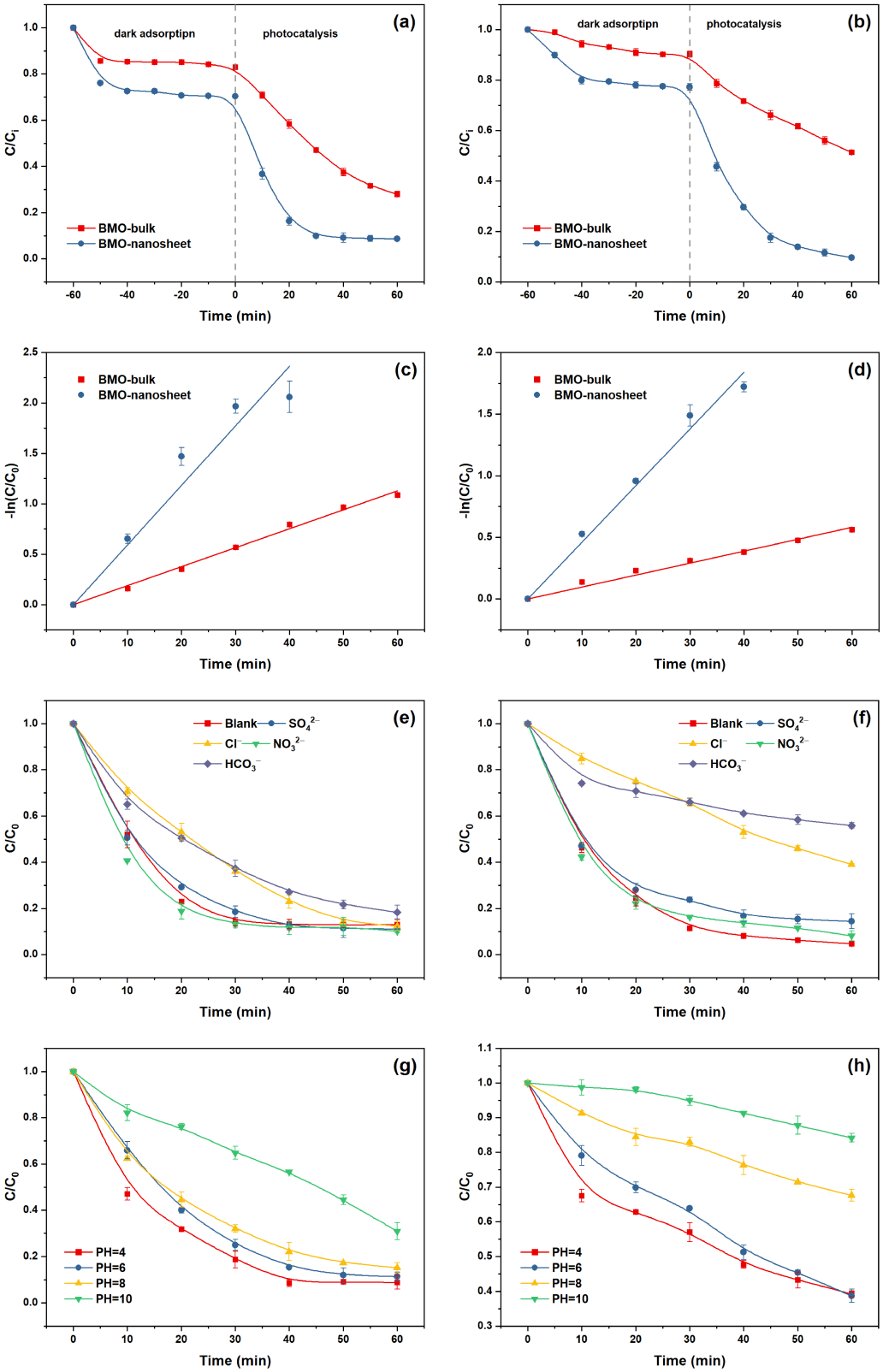


Figure 5. NPX (**a**,**c**,**e**,**g**) and IBP (**b**,**d**,**f**,**h**) removal under different experimental conditions: (**a**,**b**) dark adsorption followed by visible-light irradiation over BMO-bulk and BMO-nanosheet; (**c**,**d**) corresponding apparent pseudo-first-order kinetic plots for the irradiation stage; (**e**,**f**) effects of 1 mM coexisting anions; and (**g**,**h**) effects of initial pH over BMO-nanosheet.

2.3.2. Effects of Concentration and Water Chemistry

Increasing the initial pollutant concentration from 5 to 15 mg L^{-1} reduced removal after 60 min from 92% to 86% for NPX and from 96% to 83% for IBP (Figure S6). At a fixed catalyst loading and photon flux, higher pollutant concentrations may increase competition for surface sites and reactive species. Both compounds generally showed higher removal under acidic conditions. The point of zero charge of BMO-nanosheet was approximately 4.12, and the pKa values of NPX and IBP are 4.15 and 4.92, respectively. At pH values above both the respective pKa and the point of zero charge, electrostatic repulsion between the negatively charged catalyst surface and deprotonated NSAID anions may hinder adsorption and subsequent interfacial reactions (Figures 5g,h and S7).

Humic acid (HA, 5–15 mg L^{-1}) slowed the degradation of both compounds. At 15 mg L^{-1} HA, removal after 60 min was approximately 87% for NPX and 89% for IBP; IBP removal was about 94% without HA (Figure S8). The inhibition may result from light screening, competitive adsorption, and scavenging of reactive species by dissolved organic matter. The effects of 1 mM coexisting anions depended on the pollutant (Figure 5e,f). For NPX, NO_3^- and SO_4^{2-} had little effect on removal after 60 min, whereas Cl^- and HCO_3^- reduced removal at the early sampling times; HCO_3^- produced the highest residual NPX concentration at 60 min. For IBP, NO_3^- had little effect, whereas SO_4^{2-}, Cl^-, and HCO_3^- reduced removal to approximately 85%, 60%, and 44%, respectively. Competition for surface sites and scavenging of reactive species may have contributed to these pollutant-dependent effects, consistent with matrix-ion effects reported for another photocatalytic system [26].

2.3.3. Reusability, Degradation in Reservoir Water, and Mineralization

BMO-nanosheet showed similar NPX and IBP removal across five cycles at a fixed catalyst dosage of 20 mg per cycle (Figure 6). Catalyst losses during recovery were compensated using recovered material with the same cycling history, as described in Text S2. Post-cycle TEM and XRD showed retention of the sheet-like morphology and orthorhombic phase (Figure S9). XPS spectra collected before and after cycling showed similar Bi 4f, Mo 3d, and O 1s peak positions and profiles (Figure S10), suggesting that the predominant surface chemical states were largely retained. After 60 min of photocatalytic treatment, the mean Bi and Mo concentrations in the aqueous phase were 6.23 and 3.77 μg L^{-1} for NPX, and 8.40 and 5.40 μg L^{-1} for IBP, respectively (Table S5), indicating limited release of these elements under the tested conditions. Br was not detected in the aqueous samples collected after 60 min of photocatalytic treatment. Together, these results indicate that the morphology, crystal phase, and predominant surface chemical states of BMO-nanosheet were largely retained under the tested conditions.

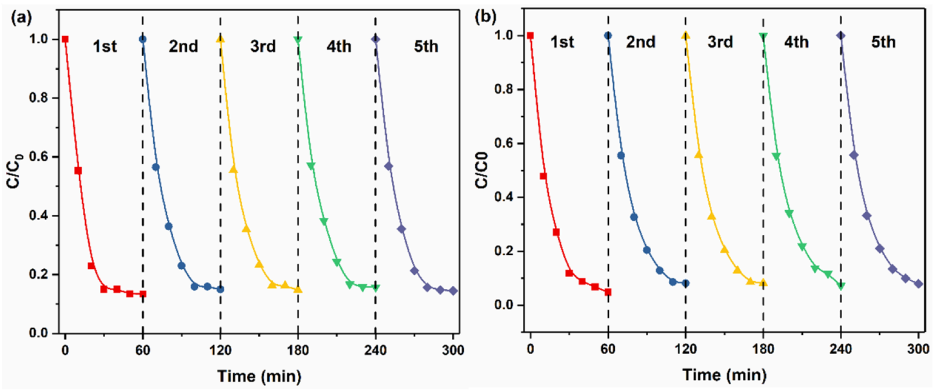


Figure 6. Five-cycle reuse experiments for visible-light degradation of (**a**) NPX and (**b**) IBP over BMO-nanosheet.

To examine matrix effects, raw water from a reservoir (Zhejiang, China; Table S6) was spiked with 10 mg L^{-1} NPX or IBP. Compared with ultrapure water, removal after 60 min decreased from 90% to 69% for NPX and from 96% to 52% for IBP. The corresponding apparent rate constants decreased from 0.059 to 0.022 min^{-1} for NPX and from 0.058 to 0.014 min^{-1} for IBP (Figure S11), with the fitted rate constants, standard errors, and R^2 values provided in Table S7. The lower photocatalytic activity in reservoir water may arise from the combined effects of dissolved organic matter and coexisting inorganic ions, which can compete with the target pollutants for reactive species and surface sites. Light attenuation by the water matrix may also reduce effective irradiation of the catalyst. The greater inhibition observed for IBP is consistent with its stronger response to several coexisting anions in the individual-ion experiments. These experiments provide a controlled comparison of water-matrix effects at the tested pollutant and ion concentrations. The 10 mg L^{-1} pollutant spike and the individual-anion tests at 1 mM were not intended to reproduce environmentally relevant pharmaceutical concentrations or the actual reservoir-water composition. Accordingly, the results are interpreted as evidence of matrix effects under the tested conditions, rather than as a demonstration of treatment performance under representative environmental conditions. The extent of parent-compound removal was substantially greater than TOC removal. After 60 min, NPX and IBP removal reached 90% and 96%, respectively, whereas TOC removal was 34% and 70% (Figure 7). This difference indicates incomplete mineralization and accumulation of organic intermediates, particularly during NPX degradation. Parent concentration alone therefore does not adequately describe treatment progress; transformation products and toxicity must also be evaluated.

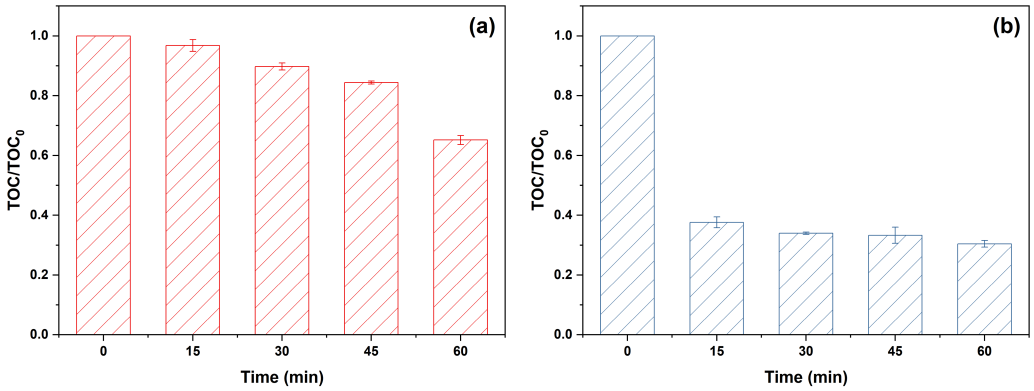


Figure 7. Total organic carbon removal during visible-light photocatalytic treatment of (**a**) NPX and (**b**) IBP over BMO-nanosheet.

2.4. Reactive Species and Photocatalytic Mechanism

2.4.1. EPR Detection of Reactive Oxygen Species

No spin-adduct signals were observed in the dark. After 5 min of visible-light irradiation, DMPO spin trapping in methanol yielded the characteristic 1:1:1:1 quartet of DMPO–$O_2^{\bullet-}$, whereas aqueous DMPO yielded the 1:2:2:1 quartet of DMPO–$^{\bullet}$OH. TEMP yielded the characteristic 1:1:1 triplet of the $^1O_2$ adduct (Figure 8). Under the respective spin-trapping conditions, all three EPR signals were stronger for BMO-nanosheet than for BMO-bulk. These results provide qualitative evidence for reactive oxygen species generation under the measurement conditions. In particular, the DMPO–$O_2^{\bullet-}$ signals were obtained in methanol, and their intensities cannot be directly translated into superoxide concentrations or contributions to pollutant degradation in the aqueous reaction system.

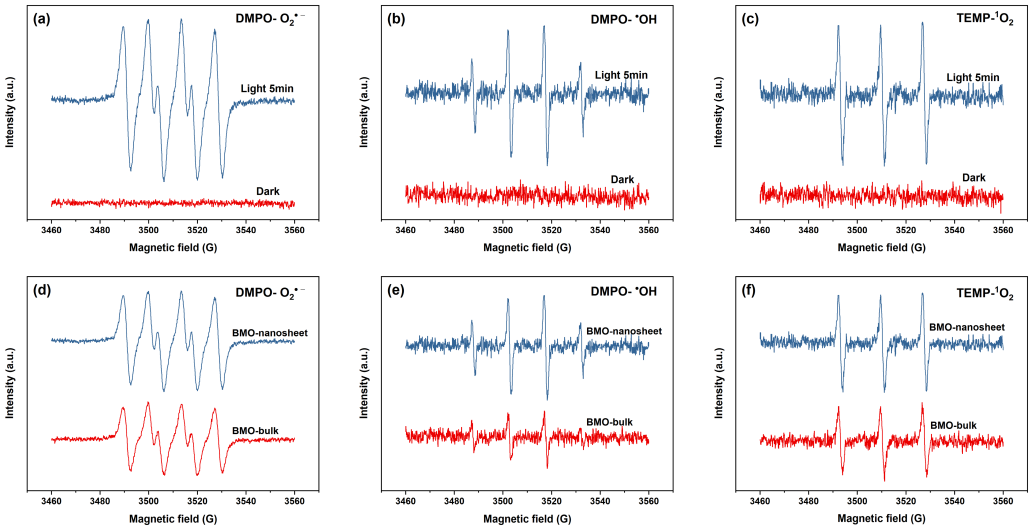


Figure 8. EPR spectra of (**a**,**d**) DMPO–$O_2^{\bullet-}$, (**b**,**e**) DMPO–$^{\bullet}$OH, and (**c**,**f**) TEMP–$^1O_2$ recorded in the dark and under visible light for BMO-bulk and BMO-nanosheet.

2.4.2. Scavenger Experiments and Mechanistic Interpretation

Scavenger experiments suggested differences in reactive-species involvement between the two pollutants (Figure 9). For NPX, the apparent rate constant without a scavenger was 0.068 min^{-1}. Isopropanol (IPA, $^{\bullet}$OH scavenger) had little effect on the apparent rate constant (0.068 min^{-1}), whereas sodium oxalate (SO, h^+ scavenger), p-benzoquinone (BQ, $O_2^{\bullet-}$ scavenger), and furfuryl alcohol (FFA, $^1O_2$ probe and scavenger) decreased the rate constant to 0.013, 0.053, and 0.023 min^{-1}, respectively. The stronger inhibition by SO and FFA is consistent with the involvement of h^+ and $^1O_2$ in NPX degradation, while the effect of BQ suggests possible involvement of $O_2^{\bullet-}$. For IBP, the rate constant without a scavenger was 0.072 min^{-1}. IPA and BQ had little effect (0.072 and 0.070 min^{-1}, respectively), whereas SO and FFA decreased the value to 0.015 and 0.021 min^{-1}. The stronger inhibition by SO and FFA likewise suggests the involvement of h^+ and $^1O_2$. The apparent rate constants and fitting statistics for the scavenging experiments are provided in Table S8. However, scavengers are not completely selective, and the observed inhibition should be interpreted qualitatively rather than as a quantitative measure of individual species contributions.

Under visible-light irradiation, electrons in BMO-nanosheet are excited from the valence band to the conduction band, leaving holes in the valence band (Figure 10). Relative to BMO-bulk, the sheet-like morphology and higher BET specific surface area of BMO-nanosheet may shorten charge-carrier transport distances and facilitate pollutant–catalyst contact, with the AFM profiles providing additional evidence of its locally thinner structure (Figure S2; Table S1) [10,20]. The estimated conduction-band potential of BMO-nanosheet (−0.75 V versus NHE) is more negative than that of BMO-bulk (−0.36 V versus NHE), providing a greater thermodynamic driving force for electron transfer to dissolved O_2. This process may generate $O_2^{\bullet-}$, with subsequent oxygen-related reactions potentially contributing to $^1O_2$ formation [10,17]. Valence-band holes may directly oxidize adsorbed NSAIDs. The scavenger results are consistent with the involvement of h^+ and $^1O_2$ in both degradation processes and suggest possible involvement of $O_2^{\bullet-}$ in NPX degradation. The limited inhibition by IPA does not support a major role for $^{\bullet}$OH under the tested conditions.

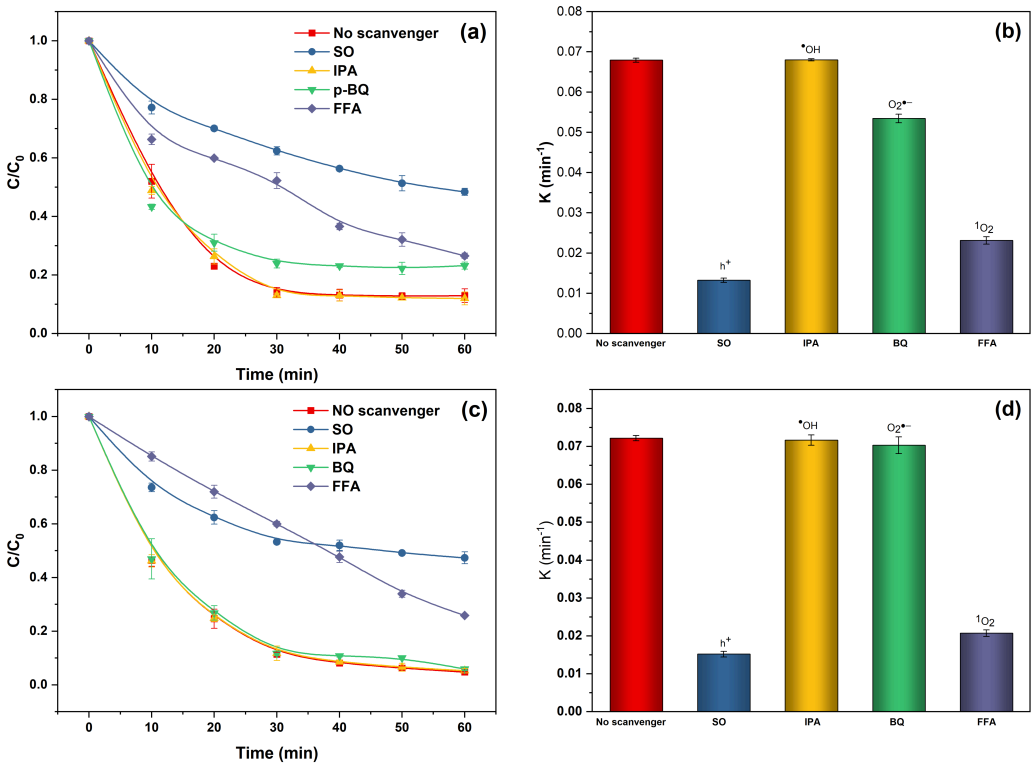


Figure 9. Effects of scavengers on the photocatalytic degradation of NPX (**a**,**b**) and IBP (**c**,**d**) over BMO-nanosheet: (**a**,**c**) degradation profiles; (**b**,**d**) apparent pseudo-first-order rate constants.

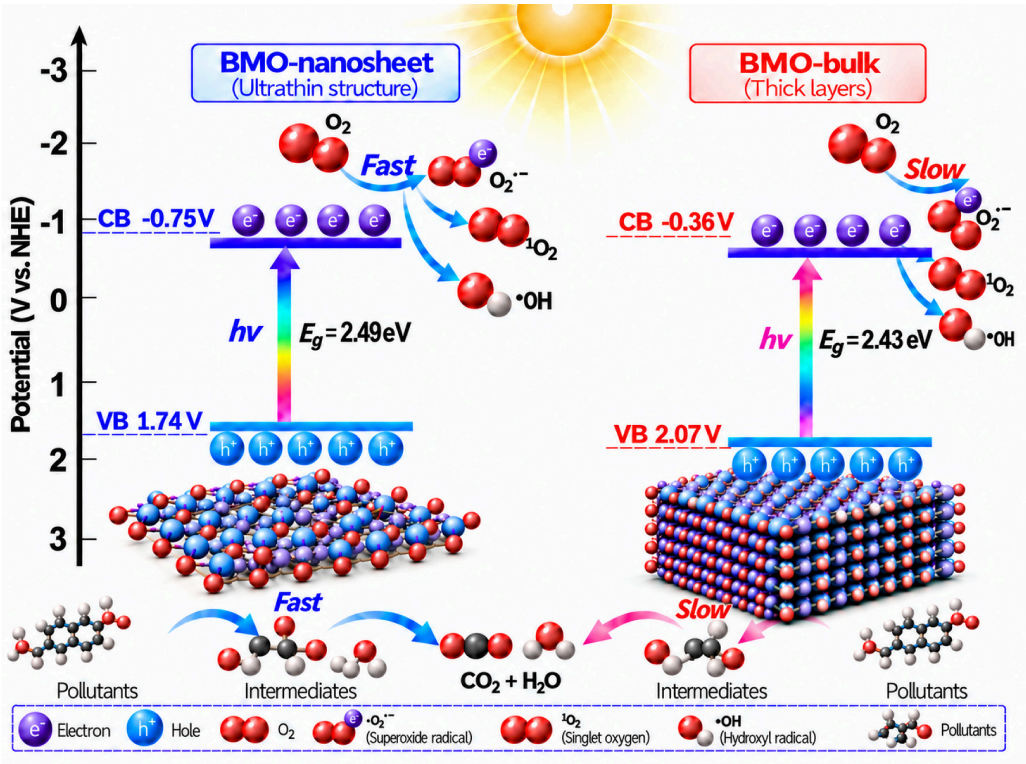


Figure 10. Proposed visible-light photocatalytic mechanisms over BMO-nanosheet and BMO-bulk (GenAI-assisted).

2.5. Transformation Products and DFT-Assisted Pathway Analysis

2.5.1. NPX Transformation Pathways

Seven NPX transformation products were assigned based on LC–MS and GC–MS analyses (Tables S9 and S10; spectra in Figures S12 and S13). DFT-based reactivity descriptors have been used to identify likely reaction sites and interpret pollutant transformation pathways [27,28]. The DFT reactivity descriptors shown in Figures 11 and 12 were calculated for neutral NPX and IBP, respectively, whereas their deprotonated forms predominate near neutral pH. Because deprotonation can alter charge distributions and site-specific reactivity, the calculated descriptors are used as qualitative aids to interpret the experimentally observed transformation products, rather than definitive predictions of reactive-site preferences in aqueous solution. Following established conceptual-DFT approaches [29,30], condensed Fukui indices calculated from Hirshfeld charges using Multiwfn [31,32] suggested C1, C2, C5, C9, C10, and C13 as potential sites for radical attack (f^0), consistent with the frontier molecular orbital distributions (Table S11; Figure 11a–e). Among the aromatic sites, C10 had the largest f^- (0.0906) and f^0 (0.0778) values and was therefore considered a likely site for hydroxylation, consistent with reported reactivity at the α-position of the naphthalene ring [33,34]. The positive electrostatic potential and positive Hirshfeld charge at the carboxyl carbon C28 suggested that this site could be susceptible to nucleophilic attack.

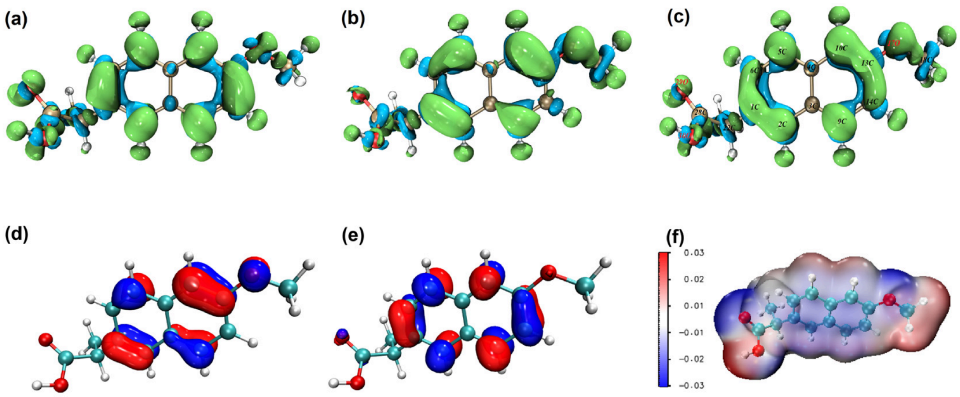


Figure 11. DFT reactivity descriptors of NPX: (**a**–**c**) Fukui-function isosurfaces (f^+, f^-, and f^0, respectively; isovalue = 0.002 a.u.); (**d**) HOMO and (**e**) LUMO (isovalue = 0.05 a.u.); and (**f**) molecular electrostatic potential.

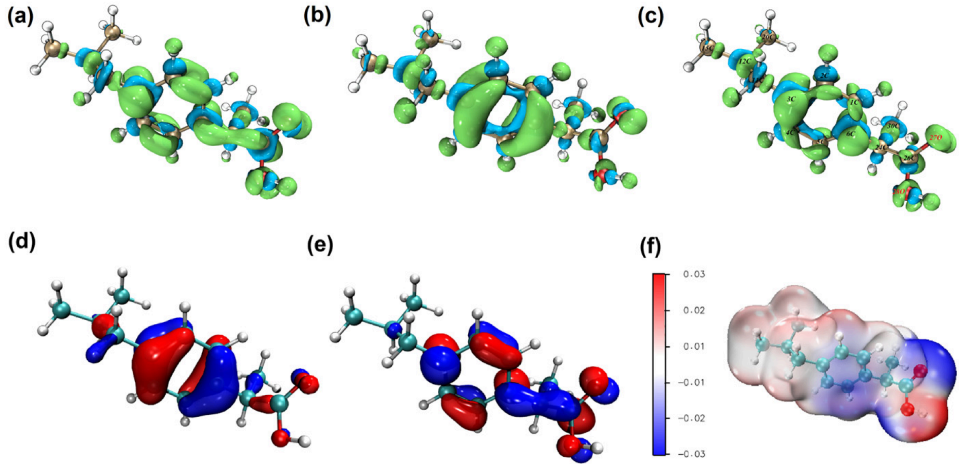


Figure 12. DFT reactivity descriptors of IBP: (**a**–**c**) Fukui-function isosurfaces (f^+, f^-, and f^0, respectively; isovalue = 0.003 a.u.); (**d**) HOMO and (**e**) LUMO (isovalue = 0.05 a.u.); and (**f**) molecular electrostatic potential.

The proposed NPX pathway begins with two principal reactions (Figure 13a). Hydroxylation was assigned to P2 (m/z 245; $C_{14}H_{14}O_4$) and decarboxylation to P1 (m/z 185; $C_{13}H_{14}O$). P1 was proposed to undergo hydroxylation and oxidation to form P3, P4, and P5, β-elimination to form P6, or cleavage of the C1–C22 bond to form P7. These assignments and subsequent reactions are consistent with reported NPX photoproducts [35–38]. Further ring oxidation and bond cleavage may produce smaller molecules and inorganic carbon, but the TOC removal of 34% after 60 min indicates that substantial organic carbon remained at the standard endpoint.

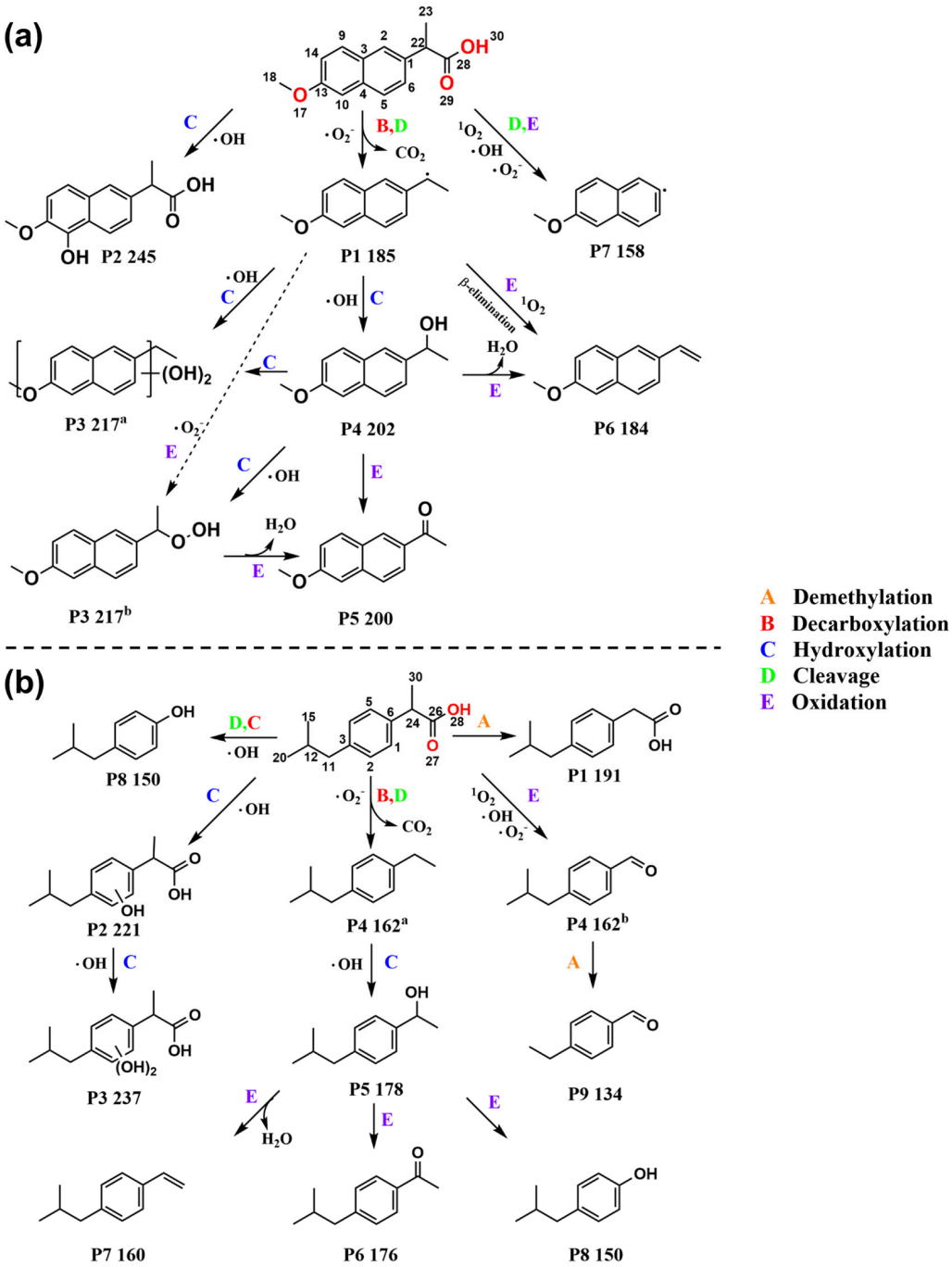


Figure 13. Proposed photocatalytic transformation pathways of NPX (**a**) and IBP (**b**) over BMO-nanosheet.

2.5.2. IBP Transformation Pathways

Nine IBP transformation products (P1–P9) were identified by LC–MS and GC–MS analyses (Tables S12 and S13; spectra in Figures S14 and S15), with alternative candidate structures proposed for P4. Fukui indices and frontier molecular orbitals suggested that the aromatic ring and carboxyl group were potentially reactive regions, particularly C3 and C6 for radical attack and C26 for nucleophilic attack (Table S14; Figure 12). The largest relevant indices were $f^0 = 0.0920$ at C3, $f^0 = 0.0820$ at C6, and $f^+ = 0.0732$ at C26.

The proposed IBP transformation pathways involve hydroxylation, decarboxylation, oxidation, demethylation, and side-chain cleavage (Figure 13b). P2 (m/z 221; $C_{13}H_{18}O_3$) and P3 (m/z 237; $C_{13}H_{18}O_4$) were assigned as hydroxylated products. For P4 at nominal m/z 162, $C_{12}H_{18}$ and $C_{11}H_{14}O$ were proposed as alternative candidate formulas, which could not be uniquely distinguished using the available evidence. The proposed transformations involving P4 and P5–P7 are therefore regarded as possible pathways. Demethylation was proposed to account for P1 (m/z 191) and to contribute to P9 formation [39]. The higher TOC removal for IBP than for NPX after 60 min indicates more extensive mineralization of IBP-derived organic carbon.

2.6. Changes in Toxicity During Photocatalysis

CHO-K1 cell viability initially decreased even as the concentrations of the parent compounds declined (Figure 14). Among the sampled time points, the lowest cell viability was observed at 90 min for NPX and 60 min for IBP, suggesting that transformation products may have contributed to the increased cytotoxicity of the treated mixtures. Cell viability subsequently showed partial recovery with longer irradiation, which may reflect further transformation of these products. ECOSAR predicted greater aquatic toxicity for several tentatively identified transformation products than for their parent compounds (Tables S15 and S16). These structure-based predictions and the CHO-K1 measurements provide complementary information, as they address individual compounds and sampled mixtures, respectively, using different toxicity endpoints. Several decarboxylated NPX products, particularly P1, P6, and P7, had greater predicted toxicity than NPX. For IBP, the candidate P4 structures and P7 were among those with the highest predicted acute toxicity, whereas P5 and P6 generally showed lower predicted acute toxicity than the P4 candidates. Previous studies have also shown that NPX photoproducts can differ substantially from the parent compound in ecotoxicity [40]. These results indicate that parent-compound removal alone does not adequately represent toxicity reduction. The comparatively low TOC removal for NPX after 60 min further highlights the need to assess pollutant removal, mineralization, and toxicity together.

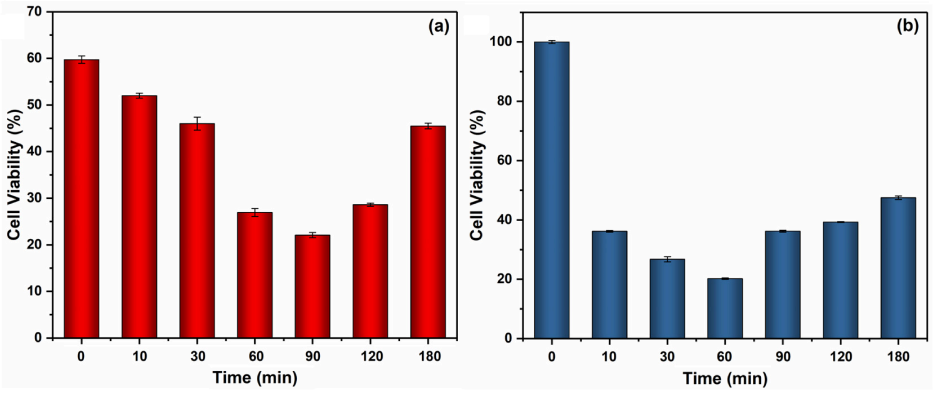


Figure 14. Changes in CHO-K1 cell viability after exposure to samples collected during visible-light photocatalytic treatment of (**a**) NPX and (**b**) IBP.

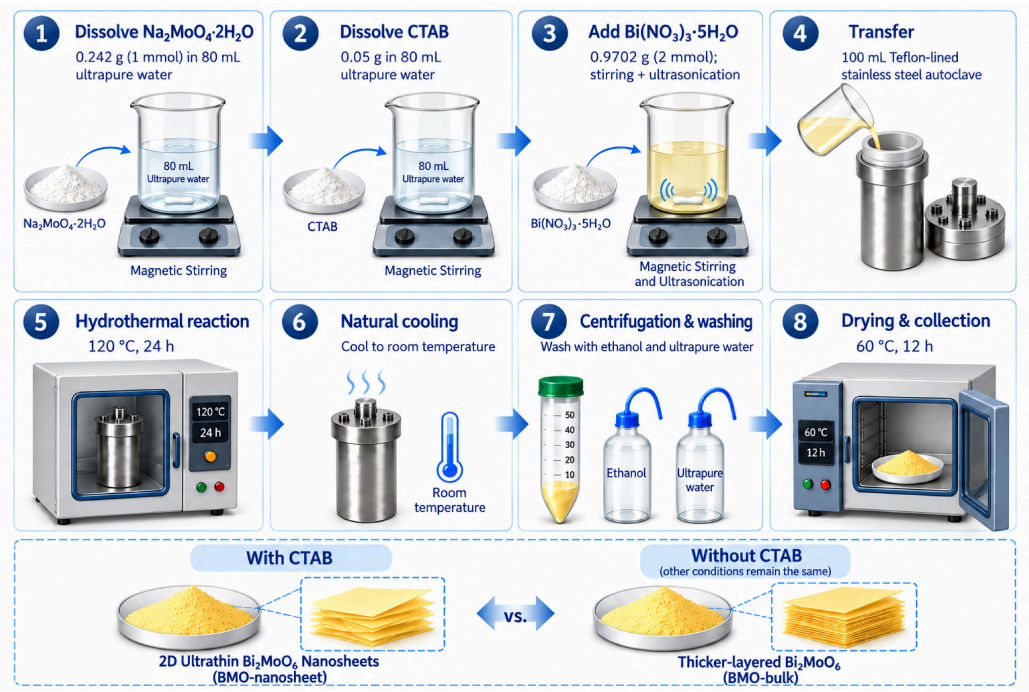
3. Materials and Methods

3.1. Chemicals and Reagents

Bismuth nitrate pentahydrate ($Bi(NO_3)_3{\cdot}5H_2O$), sodium molybdate dihydrate ($Na_2MoO_4{\cdot}2H_2O$), cetyltrimethylammonium bromide (CTAB), ethanol, methanol, sodium chloride, sodium sulfate, sodium nitrate, sodium bicarbonate, humic acid, isopropanol (IPA), p-benzoquinone (BQ), furfuryl alcohol (FFA), and sodium oxalate were of analytical grade and used without further purification. NPX, IBP, 5,5-dimethyl-1-pyrroline N-oxide (DMPO), and 2,2,6,6-tetramethylpiperidine (TEMP) were used as received. HPLC-grade solvents and ultrapure water (18.2 MΩ cm) were used for chromatographic and photocatalytic experiments. Selected physicochemical properties of NPX and IBP are summarized in Table S17.

3.2. Synthesis of BMO-Nanosheet and BMO-Bulk

$Na_2MoO_4{\cdot}2H_2O$ (0.242 g, 1 mmol) and CTAB (0.050 g) were dissolved in 80 mL of ultrapure water under magnetic stirring. $Bi(NO_3)_3{\cdot}5H_2O$ (0.9702 g, 2 mmol) was then added, and the mixture was stirred and sonicated until a pale-yellow suspension formed. The suspension was transferred to a 100 mL Teflon-lined stainless-steel autoclave and heated at 120 °C for 24 h. After the autoclave cooled naturally to room temperature, the precipitate was collected by centrifugation, washed repeatedly with ethanol and ultrapure water, and dried at 60 °C for 12 h. The resulting material was designated BMO-nanosheet. BMO-bulk was prepared by the same procedure except that CTAB was omitted. The synthesis procedure is illustrated in Scheme 1.



Scheme 1. One-step hydrothermal synthesis of BMO-nanosheet in the presence of CTAB and BMO-bulk under the same conditions without CTAB (GenAI-assisted).

3.3. Material Characterization

Morphology and microstructure were examined by SEM, TEM, and HRTEM, and elemental distributions were mapped by EDX. AFM was used to characterize surface topography and obtain height profiles, while specific surface areas were determined by the BET method using nitrogen adsorption measurements. Crystal structure and surface chemical

states were analyzed by XRD and XPS, respectively, including characterization after cycling. UV–vis absorption spectra were recorded, and optical band gaps were estimated using Tauc plots. Mott–Schottky, transient photocurrent, EIS, and steady-state PL measurements were used to investigate the electronic and charge-carrier properties. Instrument details and measurement procedures are provided in Text S1.

3.4. Photocatalytic Degradation Experiments and Analytical Methods

Photocatalytic experiments were conducted under visible light ($\lambda > 420$ nm) using a 300 W Xe lamp. Unless otherwise stated, 20 mg of catalyst was dispersed in 100 mL of NPX or IBP solution (10 mg L^{-1}) at 25 °C. For the catalyst-comparison experiments, suspensions were stirred in the dark for 60 min before irradiation for a further 60 min. The combined adsorption–irradiation profiles were expressed as C/C_i, where C_i is the initial pollutant concentration before dark adsorption. Irradiation time zero was defined as the onset of illumination. The remaining photocatalytic experiments were conducted without preliminary dark equilibration. Samples collected at selected intervals were filtered through 0.22 μm membranes and analyzed by HPLC. Apparent pseudo-first-order rate constants were obtained by fitting $-\ln(C/C_0)$ against irradiation time with the intercept fixed at zero. For the catalyst-comparison experiments, C_0 is the measured aqueous concentration at the onset of illumination; for experiments conducted without dark equilibration, C_0 is the nominal initial pollutant concentration. C denotes the measured aqueous concentration at irradiation time t. The effects of initial pollutant concentration (5–15 mg L^{-1}), pH (4–10), humic acid concentration (0–15 mg L^{-1}), and individual anions (1 mM) were examined. Catalyst reusability was evaluated over five cycles, and mineralization was assessed by aqueous TOC removal. Detailed reaction conditions, fitting intervals, catalyst recovery and reuse procedures, analytical methods, and experimental replication are provided in Text S2.

3.5. EPR and Reactive-Species Scavenging Experiments

EPR measurements were performed in the dark and after 5 min of visible-light irradiation, using DMPO to probe $O_2^{\bullet-}$ in methanol and $^{\bullet}OH$ in water, and TEMP to probe $^1O_2$ in water. Scavenging experiments employed 1.0 mM p-benzoquinone (BQ), isopropanol (IPA), furfuryl alcohol (FFA), or sodium oxalate to investigate the involvement of $O_2^{\bullet-}$, $^{\bullet}OH$, $^1O_2$, and h^+, respectively. Their effects were evaluated by comparing pollutant removal and apparent rate constants with those obtained without a scavenger. Detailed procedures and interpretation limitations are provided in Text S3.

3.6. Identification of Transformation Products and DFT Calculations

Transformation products were tentatively identified by LC–MS and GC–MS. The geometries and electronic structures of neutral NPX and IBP were calculated using Gaussian 09 at the B3LYP/6-31G(d,p) level. Condensed Fukui indices were obtained from Hirshfeld atomic charges for the N, N + 1, and N − 1 electron states using Multiwfn 3.6 [29–32]. The electron-added and electron-removed states used in these calculations are distinct from the deprotonated species formed through acid–base dissociation in water. Frontier molecular orbitals and molecular electrostatic potentials were also used to interpret reactive sites. Detailed computational procedures are provided in Text S3, and product assignments and mass spectra are presented in the Supplementary Materials.

3.7. Toxicity Assessment

Changes in cytotoxicity during photocatalytic treatment were evaluated using Chinese hamster ovary cells (CHO-K1) and a Cell Counting Kit-8 (CCK-8) assay after catalyst removal. Detailed experimental procedures are provided in Text S4. The acute and chronic

aquatic toxicity of the parent compounds and proposed transformation products was estimated using the U.S. Environmental Protection Agency's Ecological Structure–Activity Relationships (ECOSAR) program for fish, daphnids, and green algae. These predictions describe the potential toxicity of individual compounds and were interpreted separately from the cellular responses to the sampled mixtures. The predicted toxicity endpoints are reported in the Supplementary Materials.

4. Conclusions

Compared with BMO-bulk, BMO-nanosheet exhibited a two-dimensional sheet-like morphology, less aggregation, and a higher BET specific surface area. These structural features, together with photoelectrochemical responses consistent with more efficient charge separation and transfer, may contribute to the enhanced photocatalytic activity. Following 60 min of dark adsorption and 60 min of visible-light irradiation, overall removal of NPX and IBP by BMO-nanosheet reached approximately 91% and 90%, respectively. The irradiation-stage apparent rate constants were 3.1 and 4.7 times those of BMO-bulk, respectively. Similar removal was observed over five cycles at a fixed catalyst dosage. Separate water-matrix experiments showed lower removal in spiked reservoir water than in ultrapure water, particularly for IBP. EPR and scavenger results supported the involvement of h^+ and $^1O_2$, with a possible contribution from $O_2^{\bullet-}$ to NPX degradation. LC–MS/GC–MS analyses, interpreted alongside conceptual DFT descriptors, provided a basis for proposing tentative transformation pathways. Under the direct-irradiation protocol without preliminary dark equilibration, aqueous TOC removal reached 34% for NPX and 70% for IBP, indicating incomplete mineralization despite substantial parent-compound removal. CHO-K1 cell viability initially declined and subsequently partially recovered with longer irradiation, whereas ECOSAR predicted greater aquatic toxicity for some proposed products than for their parent compounds. Overall, BMO-nanosheet exhibited enhanced visible-light photocatalytic activity toward NPX and IBP under the tested conditions. The differences between parent-compound removal, TOC removal, and toxicity responses demonstrate that substantial pollutant removal did not necessarily correspond to complete mineralization or detoxification.

Supplementary Materials: The following supporting information can be downloaded at https://www.mdpi.com/article/10.3390/catal16111034/s1. Text S1: Photocatalyst characterization; Text S2: Photocatalytic and analytical procedures; Text S3: EPR, scavenging, and computational analysis; Text S4: Transformation products and toxicity; Scheme S1: Schematic illustration of the photocatalytic degradation setup (GenAI-assisted); Figure S1: SEM images of BMO-bulk and BMO-nanosheet at different magnifications; Figure S2: AFM images and corresponding height profiles of BMO-bulk and BMO-nanosheet; Figure S3: Equivalent circuit used for EIS fitting; Figure S4: EIS Nyquist plots and equivalent-circuit fits under dark and illuminated conditions; Figure S5: Removal of NPX and IBP under visible-light irradiation in the absence of a catalyst; Figure S6: Effects of initial NPX and IBP concentrations on visible-light degradation over BMO-nanosheet; Figure S7: Zeta potential of BMO-nanosheet as a function of pH; Figure S8: Effects of humic acid concentration on NPX and IBP degradation over BMO-nanosheet; Figure S9: TEM image of BMO-nanosheet after cycling and XRD patterns before and after five photocatalytic reuse runs; Figure S10: XPS spectra of BMO-nanosheet before and after cycling; Figure S11: Degradation profiles and corresponding kinetic plots for NPX and IBP in ultrapure water and spiked reservoir water; Figure S12: Negative-ion LC–MS/MS spectra of NPX transformation products; Figure S13: GC–MS spectra of NPX transformation products; Figure S14: Negative-ion LC–MS/MS spectra of IBP transformation products; Figure S15: GC–MS spectra of IBP transformation products; Table S1: BET specific surface areas of BMO-bulk and BMO-nanosheet; Table S2: Apparent charge-transfer resistance obtained from equivalent-circuit fitting of EIS spectra; Table S3: Kinetic parameters for NPX and IBP removal under visible-light irradiation; Table S4: Comparison of BMO-nanosheet with representative reported photocatalysts for NPX and IBP removal

under visible-light irradiation; Table S5: Bi and Mo concentrations in the aqueous phase after 60 min of photocatalytic treatment over BMO-nanosheet; Table S6: Main physicochemical characteristics of raw reservoir water; Table S7: Kinetic parameters for NPX and IBP removal in ultrapure and reservoir water; Table S8: Kinetic parameters for NPX and IBP removal in the presence of different scavengers; Table S9: NPX transformation products detected by LC–MS; Table S10: NPX transformation products detected by GC–MS; Table S11: Hirshfeld charges and condensed Fukui indices of NPX; Table S12: IBP transformation products detected by LC–MS; Table S13: IBP transformation products detected by GC–MS; Table S14: Hirshfeld charges and condensed Fukui indices of IBP; Table S15: ECOSAR-predicted acute and chronic toxicity of NPX and its products; Table S16: ECOSAR-predicted acute and chronic toxicity of IBP and its products; Table S17: Physicochemical properties of the target NSAIDs.

Author Contributions: Conceptualization, K.F. and H.D.; methodology, K.F.; software, K.F.; validation, K.F.; formal analysis, K.F.; investigation, K.F.; data curation, K.F.; writing—original draft preparation, K.F.; writing—review and editing, K.F., P.J., and N.L.; visualization, K.F.; supervision, P.Y. and H.M.; project administration, K.F. and Y.L.; funding acquisition, K.F., M.F., and Y.L. All authors have read and agreed to the published version of the manuscript.

Funding: This research was funded by the Shaanxi Provincial Key Industrial Chain Project (grant No. 2024SF-ZDCYL-05-03 [STY2024xz064]), the Technology Program of PowerChina Northwest Engineering Corporation Limited (grant No. RD12182-KJB-bshkygzz), the Natural Science Basic Research Program of Shaanxi (Program No. 2025JC-YBQN-955), and the Shaanxi Provincial Post-doctoral Research Funding Program (grant No. 2023BSHGZZHQYXMZZ45 [STY2024xz025]). The article processing charge (APC) was funded by the Shaanxi Provincial Postdoctoral Research Funding Program (grant No. 2023BSHGZZHQYXMZZ45 [STY2024xz025]) and the Shaanxi Provincial Key Industrial Chain Project (grant No. 2024SF-ZDCYL-05-03 [STY2024xz064]).

Data Availability Statement: All data presented in this study are included in the manuscript and the Supplementary Materials.

Acknowledgments: During the preparation of this manuscript, the authors used OpenAI's image generation tool (ChatGPT Images 2.5, OpenAI) for the purposes of assisting in the preparation of the experimental apparatus schematic, material synthesis process diagram, and proposed degradation mechanism diagram. The authors have reviewed and edited the output and take full responsibility for the content of this publication.

Conflicts of Interest: The authors declare no conflicts of interest.

Abbreviations

The following abbreviations are used in this manuscript:

AMF	atomic force microscopy
a.u.	atomic units or arbitrary units
BET	Brunauer–Emmett–Teller
B3LYP	Becke three-parameter Lee–Yang–Parr hybrid functional
BMO	bismuth molybdate (Bi_2MoO_6)
BQ	p-benzoquinone
CCK-8	Cell Counting Kit-8
CHO-K1	Chinese hamster ovary K1 cell line
CTAB	cetyltrimethylammonium bromide
DFT	density functional theory
DMPO	5,5-dimethyl-1-pyrroline N-oxide
ECOSAR	Ecological Structure–Activity Relationships
EDX	energy-dispersive X-ray spectroscopy
EIS	electrochemical impedance spectroscopy
EPR	electron paramagnetic resonance
FFA	furfuryl alcohol
GC–MS	gas chromatography–mass spectrometry
HA	humic acid

HOMO	highest occupied molecular orbital
HPLC	high-performance liquid chromatography
HRTEM	high-resolution transmission electron microscopy
IBP	ibuprofen
IPA	isopropanol
JCPDS	Joint Committee on Powder Diffraction Standards
LC–MS	liquid chromatography–mass spectrometry
LUMO	lowest unoccupied molecular orbital
NPX	naproxen
NSAIDs	non-steroidal anti-inflammatory drugs
PL	photoluminescence
SEM	scanning electron microscopy
SO	sodium oxalate
TEMP	2,2,6,6-tetramethylpiperidine
TEM	transmission electron microscopy
TOC	total organic carbon
UV–vis	ultraviolet–visible
XPS	X-ray photoelectron spectroscopy
XRD	X-ray diffraction

References

1. Huynh, N.C.; Nguyen, T.T.T.; Nguyen, D.T.C.; Tran, T.V. Occurrence, toxicity, impact and removal of selected non-steroidal anti-inflammatory drugs (NSAIDs): A review. *Sci. Total Environ.* **2023**, *898*, 165317. [CrossRef] [PubMed]
2. Lin, J.-Y.; Zhang, Y.; Bian, Y.; Zhang, Y.-X.; Du, R.-Z.; Li, M.; Tan, Y.; Feng, X.-S. Non-steroidal anti-inflammatory drugs (NSAIDs) in the environment: Recent updates on occurrence, fate, hazards and removal technologies. *Sci. Total Environ.* **2023**, *904*, 166897. [CrossRef] [PubMed]
3. Rastogi, A.; Tiwari, M.K.; Ghangrekar, M.M. A review on environmental occurrence, toxicity and microbial degradation of non-steroidal anti-inflammatory drugs. *J. Environ. Manag.* **2021**, *300*, 113694. [CrossRef] [PubMed]
4. Pires, P.; Pereira, A.M.P.T.; Pena, A.; Silva, L.J.G. Non-steroidal anti-inflammatory drugs in the aquatic environment and bivalves: The state of the art. *Toxics* **2024**, *12*, 415. [CrossRef] [PubMed]
5. Zhao, Y.; Hu, L.; Hou, Y.; Wang, Y.; Peng, Y.; Nie, X. Toxic effects of environmentally relevant concentrations of naproxen exposure on *Daphnia magna* including antioxidant system, development, and reproduction. *Aquat. Toxicol.* **2024**, *266*, 106794. [CrossRef] [PubMed]
6. Kwak, K.; Ji, K.; Kho, Y.; Kim, P.; Lee, J.; Ryu, J.; Choi, K. Chronic toxicity and endocrine disruption of naproxen in freshwater waterfleas and fish, and steroidogenic alteration using H295R cell assay. *Chemosphere* **2018**, *204*, 156–162. [CrossRef] [PubMed]
7. Su, R.; Zhu, Y.; Gao, B.; Li, Q. Progress on mechanism and efficacy of heterogeneous photocatalysis coupled oxidant activation as an advanced oxidation process for water decontamination. *Water Res.* **2024**, *251*, 121119. [CrossRef] [PubMed]
8. Qi, X.-N.; Zhu, Y.-Q.; Yuan, H.; Xu, Z.-X.; Guo, H.-R.; Li, Z.-L. Latest progress based on doped-TiO_2 photocatalysis materials: Fabrication and applications. *J. Water Process Eng.* **2025**, *78*, 108791. [CrossRef]
9. Rashid, R.; Shafiq, I.; Gilani, M.R.H.S.; Maaz, M.; Akhter, P.; Hussain, M.; Jeong, K.-E.; Kwon, E.E.; Bae, S.; Park, Y.-K. Advancements in TiO_2-based photocatalysis for environmental remediation: Strategies for enhancing visible-light-driven activity. *Chemosphere* **2024**, *349*, 140703. [CrossRef] [PubMed]
10. Di, J.; Xiong, J.; Li, H.; Liu, Z. Ultrathin 2D photocatalysts: Electronic-structure tailoring, hybridization, and applications. *Adv. Mater.* **2018**, *30*, 1704548. [CrossRef] [PubMed]
11. Zhao, D.; Cai, C. Preparation of Bi_2MoO_6/Ti_3C_2 MXene heterojunction photocatalysts for fast tetracycline degradation and Cr(VI) reduction. *Inorg. Chem. Front.* **2020**, *7*, 2799–2808. [CrossRef]
12. Zheng, Y.; Zhou, T.; Zhao, X.; Pang, W.K.; Gao, H.; Li, S.; Zhou, Z.; Liu, H.; Guo, Z. Atomic interface engineering and electric-field effects in ultrathin Bi_2MoO_6 nanosheets for superior lithium-ion storage. *Adv. Mater.* **2017**, *29*, 1700396. [CrossRef] [PubMed]
13. Yang, X.; Wang, S.; Yang, N.; Zhou, W.; Wang, P.; Jiang, K.; Li, S.; Song, H.; Ding, X.; Chen, H.; et al. Oxygen vacancies induce special CO_2 adsorption modes on Bi_2MoO_6 for highly selective conversion to CH_4. *Appl. Catal. B Environ.* **2019**, *259*, 118088. [CrossRef]
14. Dai, W.; Xiong, W.; Yu, J.; Zhang, S.; Li, B.; Yang, L.; Wang, T.; Luo, X.; Zou, J.-P.; Luo, S. Bi_2MoO_6 quantum dots grown in situ on reduced graphene oxide layers: A novel electron-rich interface for efficient CO_2 reduction. *ACS Appl. Mater. Interfaces* **2020**, *12*, 25861–25874. [CrossRef] [PubMed]

15. Lv, J.; Zhang, J.; Liu, J.; Li, Z.; Dai, K.; Liang, C. Bi SPR-promoted Z-scheme Bi_2MoO_6/CdS-diethylenetriamine composite with enhanced visible-light photocatalytic hydrogen-evolution activity and stability. *ACS Sustain. Chem. Eng.* **2017**, *6*, 696–706. [CrossRef]
16. Cai, K.; Lv, S.-Y.; Song, L.-N.; Chen, L.; He, J.; Chen, P.; Au, C.-T.; Yin, S.-F. Facile preparation of ultrathin Bi_2MoO_6 nanosheets for photocatalytic oxidation of toluene to benzaldehyde under visible-light irradiation. *J. Solid State Chem.* **2019**, *269*, 145–150. [CrossRef]
17. Di, J.; Zhao, X.; Lian, C.; Ji, M.; Xia, J.; Xiong, J.; Zhou, W.; Cao, X.; She, Y.; Liu, H.; et al. Atomically thin Bi_2MoO_6 nanosheets with vacancy pairs for improved photocatalytic CO_2 reduction. *Nano Energy* **2019**, *61*, 54–59. [CrossRef]
18. Li, S.; Bai, L.; Ji, N.; Yu, S.; Lin, S.; Tian, N.; Huang, H. Ferroelectric polarization and a thin-layered structure synergistically promote CO_2 photoreduction by Bi_2MoO_6. *J. Mater. Chem. A* **2020**, *8*, 9268–9277. [CrossRef]
19. Nakate, U.T.; Patil, P.; Nakate, Y.T.; Na, S.I.; Yu, Y.T.; Hahn, Y.B. Ultrathin ternary-metal-oxide Bi_2MoO_6 nanosheets for high-performance asymmetric supercapacitor and gas-sensor applications. *Appl. Surf. Sci.* **2021**, *551*, 149422. [CrossRef]
20. Xie, Y.; Shang, X.; Liu, D.; Zhao, H.; Gu, Y.; Zhang, Z.; Wang, X. Non-noble-metal thickness-tunable Bi_2MoO_6 nanosheets for highly efficient visible-light-driven nitrobenzene reduction into aniline. *Appl. Catal. B Environ.* **2019**, *259*, 118087. [CrossRef]
21. Zhang, L.; Xu, T.; Zhao, X.; Zhu, Y. Controllable synthesis of Bi_2MoO_6 and effects of morphology and local-structure variation on photocatalytic activity. *Appl. Catal. B Environ.* **2010**, *98*, 138–146. [CrossRef]
22. Fu, K.; Pan, Y.; Ding, C.; Shi, J.; Deng, H. Photocatalytic degradation of naproxen by Bi_2MoO_6/g-C_3N_4 heterojunction photocatalyst under visible light: Mechanisms, degradation pathway, and DFT calculation. *J. Photochem. Photobiol. A Chem.* **2021**, *412*, 113235. [CrossRef]
23. Fu, K.; Pan, Y.; Ding, C.; Shi, J.; Deng, H. Reduced Graphene Oxide/$ZnIn_2S_4$ Nanocomposite Photocatalyst with Enhanced Photocatalytic Performance for the Degradation of Naproxen under Visible Light Irradiation. *Catalysts* **2020**, *10*, 710. [CrossRef]
24. Zhang, M.; Zhang, Y.; Tang, L.; Zeng, G.; Wang, J.; Zhu, Y.; Feng, C.; Deng, Y.; He, W. Ultrathin Bi_2WO_6 nanosheets loaded with g-C_3N_4 quantum dots: A direct Z-scheme photocatalyst with enhanced activity toward organic-pollutant degradation under wide-spectrum light irradiation. *J. Colloid Interface Sci.* **2019**, *539*, 654–664. [CrossRef] [PubMed]
25. Asadzadeh-Khaneghah, S.; Habibi-Yangjeh, A.; Shahedi Asl, M.; Ahmadi, Z.; Ghosh, S. Synthesis of novel ternary g-C_3N_4/SiC/C-dots photocatalysts and their visible-light-induced activities in the removal of various contaminants. *J. Photochem. Photobiol. A Chem.* **2020**, *392*, 112431. [CrossRef]
26. Xiong, P.; Hu, J. Decomposition of acetaminophen using a TiO_2/UVA/LED system. *Catal. Today* **2017**, *282*, 48–56. [CrossRef]
27. Zheng, W.; Liu, Y.; Liu, W.; Ji, H.; Li, F.; Shen, C.; Fang, X.; Li, X.; Duan, X. A novel electrocatalytic filtration system with carbon-nanotube-supported nanoscale zerovalent copper for ultrafast oxidation of organic pollutants. *Water Res.* **2021**, *194*, 116961. [CrossRef] [PubMed]
28. Yi, X.-H.; Ji, H.; Wang, C.-C.; Li, Y.; Li, Y.-H.; Zhao, C.; Wang, A.; Fu, H.; Wang, P.; Zhao, X.; et al. Photocatalysis-activated SR-AOP over PDINH/MIL-88A(Fe) composites for enhanced chloroquine-phosphate degradation: Performance, mechanism, pathways, and DFT calculations. *Appl. Catal. B Environ.* **2021**, *293*, 120229. [CrossRef]
29. Cao, J.; Ren, Q.; Chen, F.; Lu, T. Comparative study of methods for predicting reactive sites in nucleophilic reactions. *Sci. China Chem.* **2015**, *58*, 1845–1852. [CrossRef]
30. Parr, R.; Yang, W. Density-functional approach to the frontier-electron theory of chemical reactivity. *J. Am. Chem. Soc.* **1984**, *106*, 4049–4050. [CrossRef]
31. Lu, T.; Chen, F. Multiwfn: A multifunctional wavefunction analyzer. *J. Comput. Chem.* **2012**, *33*, 580–592. [CrossRef] [PubMed]
32. Lu, T. A comprehensive electron wavefunction analysis toolbox for chemists, Multiwfn. *J. Chem. Phys.* **2024**, *161*, 082503. [CrossRef] [PubMed]
33. Li, L.; Lai, C.; Huang, F.; Cheng, M.; Zeng, G.; Huang, D.; Li, B.; Liu, S.; Zhang, M.; Qin, L.; et al. Degradation of naphthalene with magnetic biochar-activated hydrogen peroxide: Synergism of biochar and Fe–Mn binary oxides. *Water Res.* **2019**, *160*, 238–248. [CrossRef] [PubMed]
34. Luo, S.; Gao, L.; Wei, Z.; Spinney, R.; Dionysiou, D.D.; Hu, W.-P.; Chai, L.; Xiao, R. Kinetic and mechanistic aspects of hydroxyl-radical-mediated degradation of naproxen and its reaction intermediates. *Water Res.* **2018**, *137*, 233–241. [CrossRef] [PubMed]
35. Tu, N.; Liu, Y.; Li, R.; Lv, W.; Liu, G.; Ma, D. Experimental and theoretical investigation of the photodegradation mechanisms of naproxen and its photoproducts. *Chemosphere* **2019**, *227*, 142–150. [CrossRef] [PubMed]
36. Liang, R.; Sun, S.S.; Huang, G.; Li, M.-D. Unveiling the photophysical and photochemical reaction processes of naproxen via ultrafast femtosecond-to-nanosecond laser flash photolysis. *Chem. Res. Toxicol.* **2019**, *32*, 613–620. [CrossRef] [PubMed]
37. Marotta, R.; Spasiano, D.; Di Somma, I.; Andreozzi, R. Photodegradation of naproxen and its photoproducts in aqueous solution at 254 nm: A kinetic investigation. *Water Res.* **2013**, *47*, 373–383. [CrossRef] [PubMed]
38. Jiménez, M.; Miranda, M.; Tormos, R. Photochemistry of naproxen in the presence of β-cyclodextrin. *J. Photochem. Photobiol. A Chem.* **1997**, *104*, 119–121. [CrossRef]

39. Wu, Z.; Chen, C.; Zhu, B.-Z.; Huang, C.-H.; An, T.; Meng, F.; Fang, J. Reactive nitrogen species are also involved in the transformation of micropollutants by the UV/monochloramine process. *Environ. Sci. Technol.* **2019**, *53*, 11142–11152. [CrossRef] [PubMed]
40. Isidori, M.; Lavorgna, M.; Nardelli, A.; Parrella, A.; Previtera, L.; Rubino, M. Ecotoxicity of naproxen and its phototransformation products. *Sci. Total Environ.* **2005**, *348*, 93–101. [CrossRef] [PubMed]

Disclaimer/Publisher's Note: The statements, opinions and data contained in all publications are solely those of the individual author(s) and contributor(s) and not of MDPI and/or the editor(s). MDPI and/or the editor(s) disclaim responsibility for any injury to people or property resulting from any ideas, methods, instructions or products referred to in the content.